Magnetic anisotropy of uniaxial ferromagnets near the Curie temperature

P. Riego,[1,2] L. Fallarino,[1] C. Martínez-Oliver,[1] and A. Berger[1]
[1]*CIC nanoGUNE BRTA, E-20018 Donostia-San Sebastián, Spain*
[2]*Departamento de Física de la Materia Condensada, Universidad del País Vasco, UPV/EHU, 48080 Bilbao, Spain*

(Received 6 April 2020; accepted 4 November 2020; published 23 November 2020)

We experimentally explore the orientation dependence of the magnetization in single-crystal $Co_{0.77}Ru_{0.23}$ alloy films and demonstrate that the material remains magnetically anisotropic near and even above the Curie temperature T_C, which is incompatible with the conventional description of anisotropy via temperature-dependent anisotropy constants. To accomplish an appropriate description of magnetic anisotropy at all temperatures, we derive an improved, but still simple free-energy description based upon the anisotropic Heisenberg model that is in excellent agreement with our experimental data.

DOI: 10.1103/PhysRevB.102.174436

I. INTRODUCTION

Magnetocrystalline anisotropy (MCA) is an essential aspect of ferromagnetism [1–15]. It defines the critical behavior of ferromagnetic (FM) systems [4] and without it, FM order would not exist in ultrathin films [16–19]. For applications, FM materials are often selected based upon their MCA properties, as some technologies demand very stable remanent magnetization states, such as in hard magnets or data storage [20–24], and others require optimized susceptibilities as in transformers, for instance [25]. Recently, the relevance of MCA for the stability of skyrmions has been addressed [26,27] and its electrical control has been enabled [28], illustrating the continued relevance of MCA as a crucial research topic.

In the past two decades, substantial progress has been made related to the theoretical description of MCA and sophisticated first-principle calculation methods have been developed to compute its values and even its temperature dependence accurately, including cases of complex materials and nonmonotonic behavior [11,29,30]. However, even these most advanced methodologies, which are theoretically and computationally demanding, are generally mapped for analysis purposes onto a free-energy density description that is dependent on the orientation of the order parameter [3,11,28,29]:

$$\mathcal{F}(T) = K_0(T) + \sum_n K_n(T) \cdot f_n(\hat{m}_x,\ \hat{m}_y,\ \hat{m}_z), \qquad (1)$$

for which $K_0(T)$ is the orientation-independent FM energy, $f_n(\hat{m}_x,\ \hat{m}_y,\ \hat{m}_z)$ are functions describing the symmetry of the system via projections $\hat{m}_i$ of the normalized magnetization vector $\hat{\boldsymbol{m}}$ onto Cartesian coordinates, and $K_n(T)$ are anisotropy constants. Equation (1) is defined in the absence of a magnetic field but, in practice, an external magnetic field is necessary to align the magnetization along different crystal orientations. For the here-relevant example of a system with only the lowest-order uniaxial MCA, the effect of a magnetic field can be incorporated as [3]:

$$\mathcal{F}_{K(T)}(T, H) = K_0(T) - K_1(T)\, \hat{m}_z^2 - \mu_0 M_s(T)\, \hat{\boldsymbol{m}} \cdot \boldsymbol{H}. \quad (2)$$

$K_1(T)$ is the first-order uniaxial anisotropy coefficient and the last term represents the Zeeman energy [31], where $\boldsymbol{H}$ is the applied field [32], μ_0 the vacuum permeability, and $M_s(T)$ the saturation magnetization at temperature T. The magnetic easy axis (EA) is oriented along z. In this approach $K_n(T)$ and $M_s(T)$ are assumed to be independent of $\boldsymbol{H}$, which is a sensible assumption for temperatures sufficiently below T_C. The temperature dependence of $K_n(T)$ has been predicted by using statistical models with various degrees of refinement, including detailed magnon spectra and their temperature-dependent populations [5–11], as well as even more sophisticated first-principles methods [11,28,29].

However, based upon the above definition, $K_n(T)$ will approach zero as $T \to T_C$ because for formal consistency, the orientation dependence of the free energy has to disappear if the order parameter vanishes [5–11]. Given that the K_n are only T dependent, a vanishing K_n seems to suggest that, for $T \geqslant T_C$ no MCA persists. This is contradicted by experiments where anisotropic susceptibility (AS) was observed in the thermodynamic paramagnetic (PM) state [33–36]. For uniaxial symmetry specifically, one finds in the PM regime that the free-energy density can be described as [37]

$$\mathcal{F}_{\mathrm{AS}}(T, H) = -\frac{\mu_0 M_s^0}{2} \chi_{\parallel}(T)\, H_{\parallel}^2 - \frac{\mu_0 M_s^0}{2} \chi_{\perp}(T)\, H_{\perp}^2, \quad (3)$$

where $\chi_{\parallel} \neq \chi_{\perp}$ are the T-dependent susceptibilities parallel and perpendicular to the EA, respectively, $H_{\parallel}$ and $H_{\perp}$ the corresponding applied field components, and M_s^0 the saturation magnetization at $T = 0$.

This paradox of $K_n(T)$ vanishing at T_C but magnetic systems retaining MCA reflects the fact that Eq. (1) is not a useful concept for the description of magnetic systems near or above T_C, where the size of the order parameter itself is greatly affected by $\boldsymbol{H}$. Thus, the conventional approach of first computing $K_n(T)$ for the magnetic-field-free case using any level of sophistication and then introducing the outcome of such calculations into Eq. (2) is bound to fail in the vicinity of T_C or in the paramagnetic regime in general. Correspondingly, our work here aims at experimentally exploring the existence

 ©2020 American Physical Society

of anisotropic magnetic behavior in the vicinity of T_C and finding a suitable model to describe these experimental observations. Specifically, we study the magnetic behavior of uniaxial ferromagnets near T_C. Samples with minute magnetostatic interactions are hereby needed to avoid domain formation [38,39] and make Eq. (2) directly applicable. Crystalline hexagonal-close-packed (hcp) $(10\bar{1}0)$ $Co_{1-x}Ru_x$ alloy thin films constitute an excellent choice, given their uniaxial MCA with an in-plane EA parallel to the hcp c axis that makes the magnetostatic energy essentially irrelevant. In addition, T_C can be tuned by varying the Ru concentration x, while conserving high crystalline quality [40–43]. Our work here focuses on $Co_{0.77}Ru_{0.23}$ alloy samples, whose $T_C = 417\,\mathrm{K}$ enabled measurements in the most relevant temperature range from $0.8 \leqslant T/T_C \leqslant 1.2$.

The paper is organized as follows: in Sec. II, we describe all key experimental aspects that were utilized in the present work. Section III describes the experimental results and the key discrepancy in between our measurements and the conventional anisotropy description according to Eqs. (2) and (3). We then derive a new model description of temperature-dependent anisotropy effects based upon a microscopic Hamiltonian that simultaneously considers both field-induced changes in the size of the magnetization as well as field-induced magnetization reorientation processes, and we demonstrate that this approach is suitable to describe all our experimental results in a quantitatively accurate manner. Section IV summarizes the conclusions of our study. Furthermore, the Appendix provides detailed information about the mathematical derivation of our model description, including a further refinement to achieve proper behavior at low temperatures, which is not the primary focus of this work.

II. EXPERIMENTAL ASPECTS

A series of uniaxial magnetic samples was fabricated onto Si (110) substrates by means of room-temperature sputter deposition utilizing a UHV system (ATC series by AJA International) with a base pressure of better than 1.2×10^{-6} Pa. By means of hydrofluoric (HF) acid etching Si (110) substrates immediately before sputter deposition, and by utilizing a suitable template layer series of Ag (75 nm), Cr (20 nm), and $Cr_{0.72}Ru_{0.28}$ (20 nm) prior to growing the ferromagnetic 50-nm-thick $Co_{0.77}Ru_{0.23}$ films, the epitaxial growth of hcp $(10\bar{1}0)$ $Co_{1-x}Ru_x$ films can be achieved [40–45]. The multilayer structure of the system is shown schematically in the inset of Fig. 1(a). Each of our samples was covered by SiO_2 for oxidation and degradation protection. The crystallographic structure of our samples and especially the proper epitaxial orientation have been investigated via x-ray diffraction (XRD) θ-2θ scans utilizing a PANalytical X'Pert Pro diffractometer with Cu Kα radiation. The magnetic characterization was performed using a commercial MicroMag 3900 vibrating sample magnetometer. The magnetometer is equipped with both a 360° rotational stage, which allows for an angular precision of better than 1°, and with a furnace, which permits temperature-dependent magnetization measurements for 293 K $\leqslant T \leqslant$ 1073 K. During the furnace operation, the sample zone was continuously evacuated by an extraction pump and filled with a constant flow of helium gas to avoid undesired chemical reactions. Moreover, to reduce temperature gradients, the oven was covered by a radiation shield, which allows reliable measurements under stable temperature conditions.

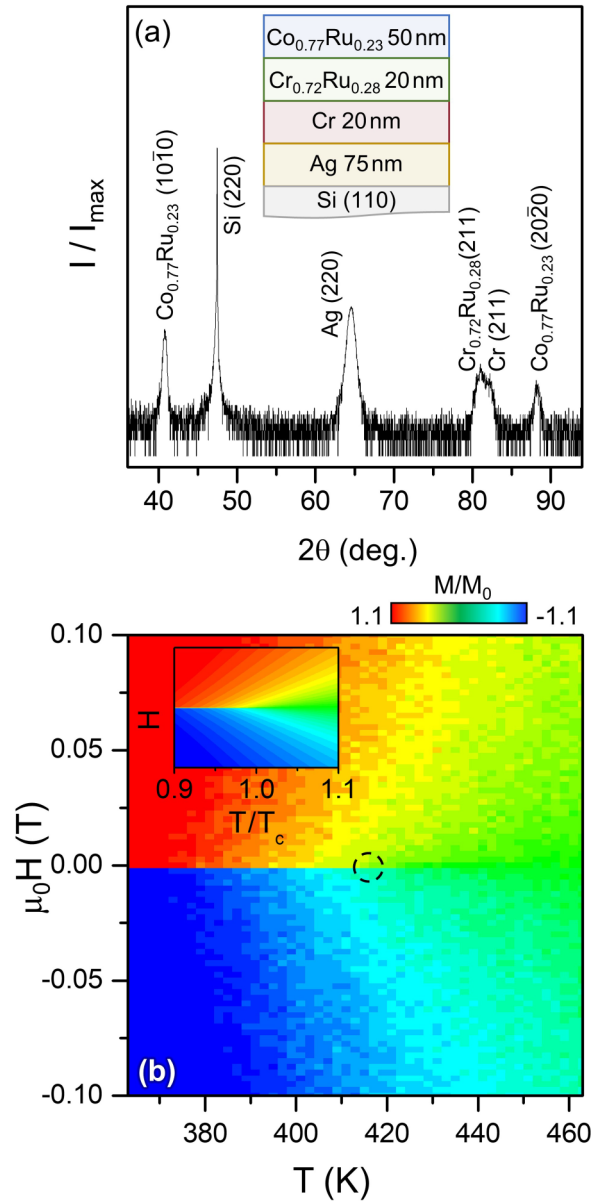

FIG. 1. (a) X-ray diffraction $\theta - 2\theta$ scan of an epitaxial $Co_{0.77}Ru_{0.23}$ film sample. Inset: multilayer structure of the sample. The sample is covered by a 10-nm-thick SiO_2 layer (not shown). (b) Measured stable-state magnetization M (in color code, normalized to M_0, the largest value occurring in the range shown) as a function of T and H, which was applied along the EA. Inset: computed magnetization as a function of T/T_C and H for the three-dimensional Ising model.

III. RESULTS AND DISCUSSION

The correct epitaxy and crystalline quality of our samples was verified by means of XRD measurements, as shown in

the main panel of Fig. 1(a). The scan exhibits only well-defined diffraction peaks corresponding to Si (220), Ag (220), Cr (211), $Cr_{0.72}Ru_{0.28}$ (211), and $Co_{0.77}Ru_{0.23}$ $(10\bar{1}0)$ crystal planes. The absence of any other diffraction peak and the fact that the higher-order $Co_{0.77}Ru_{0.23}$ $(20\bar{2}0)$ signal is clearly visible are both convincing indicators of the excellent crystallographic quality of our samples, which exhibit a uniform in-plane c-axis orientation that is defining the EA of magnetization for this alloy.

Figure 1(b) shows the measured EA magnetization of the thermodynamically stable state as a function of T and applied field strength H in the vicinity of T_C, whose value was determined by the proper scaling analysis of these magnetization data, following the scaling relation derived by Arrott and Noakes [46]. For $T < T_C$, the magnetization is nearly independent of H and only changes its sign when H switches direction, as represented by the discontinuous color change. Correspondingly, the ferromagnetic system exhibits a phase boundary along $H = 0$, whose high-temperature end defines a critical point at the Curie temperature T_C, which itself is a field-independent quantity. Above T_C, the magnetization is zero for $H = 0$ and gradually increases with H. The inset in Fig. 1(b) displays the theoretically expected $M(T,H)$ behavior of the three-dimensional Ising model [47], which is nearly identical to our experimental data, thus verifying the suitability of our sample selection to produce macroscopic film samples that behave like ideal single-domain uniaxial ferromagnets. Therefore, our samples can be directly compared with microscopic models, a fact that we will utilize in the following discussion about magnetic anisotropy in the vicinity of $T = T_C$.

To study the MCA near T_C, we measured the sample magnetization as a function of an applied field of decreasing strength H and the angle α between the EA and the applied field direction for fixed temperatures T [40,48]. Experimental results are shown in the left column of Fig. 2, where the color code represents the magnetization value M_H along the field axis. The measurements at $T = 0.8\,T_C$ in Fig. 2(a) show the prototypical behavior of a uniaxial ferromagnet. When the field is along the EA ($\alpha = 0°$, 180°), the magnetization keeps its saturation value as the field amplitude decreases. For $\alpha = 90°$ and 270°, the magnetization is parallel to the field direction for high-field values H, but as H decreases, the magnetization vector rotates towards the EA, resulting in a decrease of M_H, giving the data an archlike appearance. For $T = 0.9\,T_C$, Fig. 2(b) presents a similar behavior, even though with a slightly weaker orientation dependence of M_H. For $T > T_C$ in Figs. 2(c) and 2(d), the magnetization is zero for all α at $H = 0$ because the sample is in the PM phase. However, α-dependent features persist in $M_H(\alpha, H)$ for $H > 0$, and the sample displays relevant MCA.

Our experimental data were fitted to the $K(T)$ model according to Eq. (2), with the resulting fits being shown in the central column of Fig. 2. For $T/T_C = 0.8$ the fit in Fig. 2(e) reproduces the experimental data very well, so that the residuals of the fit, shown in Fig. 2(i), nearly vanish everywhere. However, for temperatures close to and above T_C, i.e., the datasets in Figs. 2(b)–2(d), fits to the $K(T)$ model in Figs. 2(f)–2(h) show significant deviations from the experimental data, which are especially visible in the residual plots in Figs. 2(j)–2(l). These discrepancies demonstrate that the $K(T)$ model cannot reproduce our experimental data, especially near the EA, where the $K(T)$ model fails to account for an H-dependent magnetization. The inclusion of higher-order anisotropy constants according to Eq. (1) does not resolve this discrepancy.

We furthermore fitted our $T/T_C = 1.1$ and the $T/T_C = 1.2$ datasets to the AS model of Eq. (3), which is valid for sufficiently high temperatures. However, this model also does not reproduce these data very accurately, because it does not account for still relevant nonlinear M_H vs H dependencies, including magnetization rotations. Only at yet higher T is the magnetization behavior well described by the AS model of Eq. (3).

Thus, our data show that neither the $K(T)$ nor the AS model can satisfactorily describe experimentally observed MCA near T_C. This is relevant, because experiments and applications that operate near $T = T_C$, such as pump-probe experiments or thermally assisted recording, will be crucially impacted by the evolution of MCA with T. Therefore, an improved model that overcomes the limitations of Eq. (2) and Eq. (3) is required. For its derivation, the microscopic Hamiltonian of a uniaxial ferromagnet in the presence of an external field was taken as a starting point, so that the subsequently computed equilibrium state at temperature T considers the impact of both competing energies simultaneously. Resorting to the mean-field approximation (MFA), we calculated the corresponding free energy, from which self-consistent equations for the magnetization components resulted as described in detail in the Appendix.

The energy density of a ferromagnet with single-ion first-order uniaxial MCA in the presence of an applied field is

$$\mathcal{H} = -\frac{1}{N}\sum_{i<j}^{N,N} J\boldsymbol{S}_i \cdot \boldsymbol{S}_j + \frac{1}{N}\sum_{i}^{N} \kappa\left[1 - \left(S_i^z\right)^2\right] - \frac{\mu_0 M_s^0}{N}\sum_{i}^{N} \boldsymbol{H} \cdot \boldsymbol{S}_i. \tag{4}$$

Hereby, $\boldsymbol{S}_i$ and $\boldsymbol{S}_j$ are spin operators (or unit vectors along the direction of the spin, in the classical approach) of the i^{th} and j^{th} out of N total spins in the system. The first term in Eq. (4) accounts for the isotropic Heisenberg FM exchange with $J > 0$ for spins on neighboring lattice sites, the second term represents the uniaxial MCA energy of strength $\kappa > 0$, which originates from the spin-orbit coupling of the ferromagnetic material [49] and favors a spin alignment along $\hat{\boldsymbol{z}}$, and the last term is the Zeeman energy. If dipole-dipole interactions are neglected, $\boldsymbol{H}$ and the thermal averages of $\boldsymbol{S}_i$ and $\boldsymbol{S}_j$ can be assumed to lie within the xz plane without loss of generality, which corresponds to the film plane in our experiments. J and κ are temperature-independent constants.

Within the vectorial mean-field approximation (VMFA), derived here and described in detail in the Appendix, and furthermore assuming translational invariance, Eq. (4) simplifies to

$$\mathcal{H}_{\text{VMFA}} = \tfrac{1}{2} qJ\langle \boldsymbol{S}\rangle^2 + \kappa(1 + (\hat{\boldsymbol{z}} \cdot \langle \boldsymbol{S}\rangle)^2) - \boldsymbol{H}^{\text{eff}} \cdot \boldsymbol{S}, \tag{5}$$

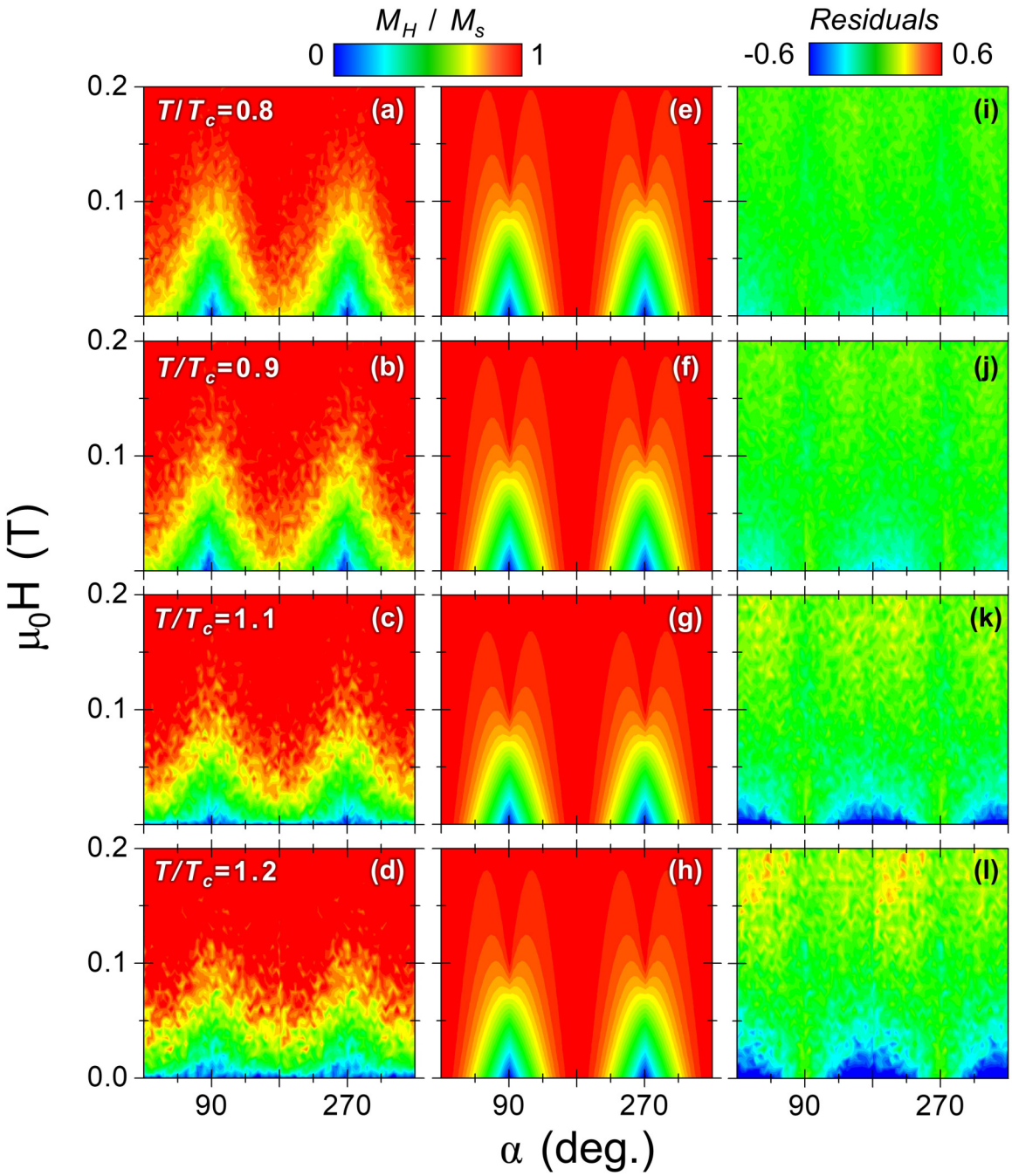

FIG. 2. (a)–(d): Field-projected magnetization $M_H = M_\parallel \cos\alpha + M_\perp \sin\alpha$, normalized to $M_s(T)$, measured as a function of α and H for different T/T_C (the actual measurement range is hereby $\alpha = 0$–180° while the displayed range covers a full rotation for visual clarity); (e)–(h): Least-squares fit of Eq. (2) to the datasets shown in (a)–(d), respectively; (i)–(l): Residuals maps, i.e., difference between experimental data and fits for different T/T_c.

with

$$\boldsymbol{H}^{\text{eff}} = qJ\langle \boldsymbol{S}\rangle + 2\kappa(\hat{z}\cdot\langle \boldsymbol{S}\rangle)\hat{z} + \mu_0 M_s^0 \boldsymbol{H}, \tag{6}$$

and $\langle \boldsymbol{S}\rangle$ being the thermodynamic average of $\boldsymbol{S}$, which is proportional to the magnetization $\boldsymbol{M}$. The case we consider here is that of a classical spin, which yields a free energy

$$\mathcal{F}_{\text{VMFA}}(T,H) = \mathcal{C} - \frac{1}{\beta}\ln\left(\frac{\sinh(\beta H^{\text{eff}})}{\beta H^{\text{eff}}}\right), \tag{7}$$

where H^{eff} is the modulus of $\boldsymbol{H}^{\text{eff}}$ given by Eq. (6), $\mathcal{C}$ is a function independent of $\boldsymbol{H}^{\text{eff}}$, and $\beta = 1/k_B T$. The magnetization components parallel and perpendicular to the EA can now be determined through

$$\frac{M_\nu}{M_s^0} = \langle S_\nu\rangle = \left(\coth(\beta H^{\text{eff}}) - \frac{1}{\beta H^{\text{eff}}}\right)\frac{H_\nu^{\text{eff}}}{H^{\text{eff}}}, \tag{8}$$

where $\nu = \parallel, \perp$. Given that H^{eff} depends on both $\langle S_\nu\rangle$, the equations for $\nu = \parallel$ and $\nu = \perp$ are coupled and need to be

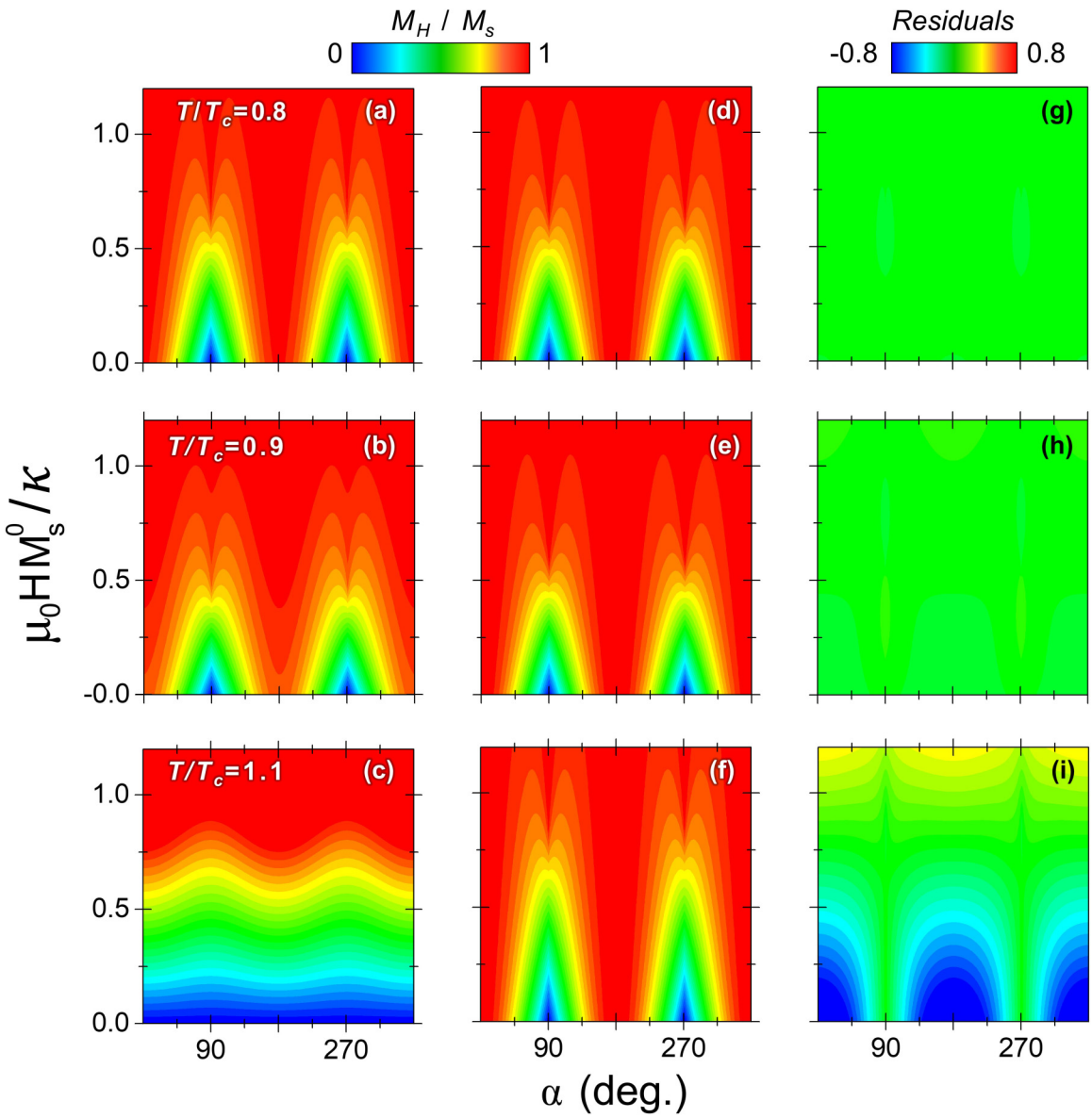

FIG. 3. (a)–(c) Field-projected magnetization $M_H = M_\parallel \cos\alpha + M_\perp \sin\alpha$, computed using Eq. (8), normalized to $M_s(T)$, as a function of magnetic field orientation and amplitude for different T/T_C. (d)–(f) Least-squares fit of Eq. (2) to the datasets shown in (a)–(c), respectively. (g)–(i) Corresponding residuals maps.

solved self-consistently, as described in more detail in the Appendix.

Equation (8) was solved numerically for different values of H and α for a wide range of temperatures and the resulting $M_H(\alpha, H)$ simulation data were analyzed. Selected plots are shown in the left column of Fig. 3. A comparison between the displayed calculations in Fig. 3 and the experimental data in Fig. 2 yields an excellent qualitative correspondence further corroborated by the fits of the VMFA model data in Figs. 3(a)–3(c) to the $K(T)$ model. The fit in Fig. 3(d) and the residuals in Fig. 3(g) reveal that the $T/T_C = 0.8$ VMFA simulation data are well described by the $K(T)$ model, i.e., the VMFA model has the $K(T)$ model as its low-temperature limit. For higher T, the VMFA model reproduces the experimentally observed nonvanishing longitudinal susceptibility, which cannot be fitted by the $K(T)$ model. In particular, the VMFA model data for $T/T_C = 1.1$ in Fig. 3(c) show the same features as the experimental data in Fig. 2(c), including the characteristic behavior of the residuals in Fig. 3(i) and Fig. 2(k), respectively.

All calculated VMFA $M_H(\alpha, H)$ datasets were fitted using the $K(T)$ model and the AS model. The corresponding coefficients of determination R^2, which symbolize the matching of the various theoretical models with each other, are shown in Fig. 4(a) as a function of T. For low T, VMFA becomes indistinguishable from the conventional $K(T)$ model, as shown by $R^2 \to 1$, given that the dominant field-induced process is magnetization rotation. At high $T > T_C$, the field response is well described by a linear susceptibility tensor and VMFA converges to the AS model. For T close to T_C the magnetization vector rotates and changes its size simultaneously when applying a field, and neither $K(T)$ nor AS model fit the data.

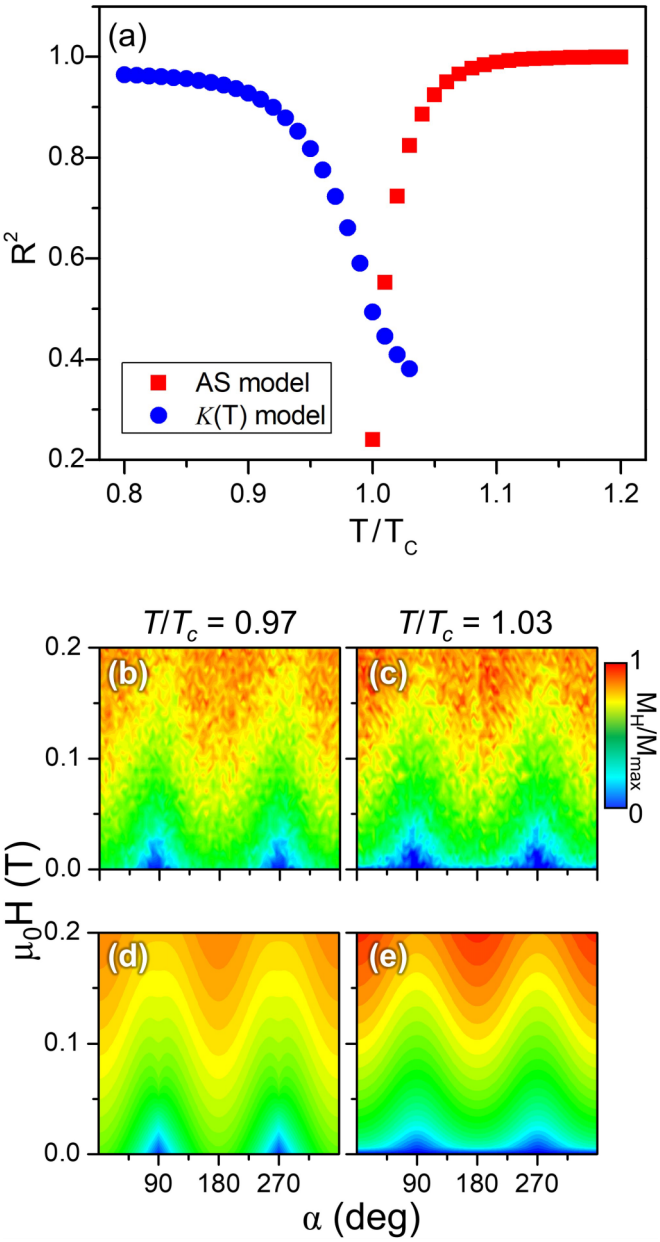

FIG. 4. (a) Coefficient of determination R^2 for the fits of computed $M_H(\alpha, H)$ datasets using the VMFA model of Eq. (8) to the $K(T)$ model (blue circles) and the AS model (red squares), as a function of temperature. (b), (c) Experimental $M_H(\alpha, H)$ datasets for $T/T_C = 0.97$ and $T/T_C = 1.03$, respectively, with the magnetization normalized to the maximum measured value (the actual measurement range is hereby $\alpha = 0$–180° while the displayed range covers a full rotation for visual clarity). (d), (e) Corresponding maps utilizing the VMFA model of Eq. (8) for $T/T_C = 0.97$ and $T/T_C = 1.03$.

Our experimental data show the same trend as the VMFA model calculations. Table I shows R^2 values for the fits of several representative experimental datasets in the vicinity of T_C to all three models. The quality of the experimental data fits to the $K(T)$ model decreases as T/T_C gets larger, while the fits to the AS model are only viable for $T > T_C$ and neither model can reproduce our experimental data in the vicinity of T_C. The appropriateness of the VMFA model on the other hand

TABLE I. R^2 for least-squares fits of selected experimental data [shown in Figs. 2(b), 2(c), 4(b), and 4(c)] to the $K(T)$ model, Eq. (2), the AS model, Eq. (3), and the VMFA model, Eq. (8).

T/T_c	R^2 $K(T)$ model	R^2 AS model	R^2 VMFA model
0.9	0.772 21	No convergence	0.932 67
0.97	0.701 13	No convergence	0.876 12
1.03	0.590 67	0.045	0.919 42
1.1	0.468 53	0.208	0.918 55

is corroborated by the high R^2 values that we find for fits to the experimental $M_H(\alpha, H)$ data for all T/T_C ratios, including those in the close vicinity of $T = T_C$.

Figures 4(b) and 4(c) show experimental $M_H(\alpha, H)$ plots for two temperatures close to T_C, and the respective fits to the VMFA model are shown in Figs. 4(d) and 4(e). The fits capture all relevant features of the orientation-dependent magnetization in a quantitatively accurate manner. Specifically, the VMFA model accounts for the vanishing magnetization at $H = 0$ and $T > T_C$ and the nonvanishing longitudinal susceptibility, which cannot be described by the $K(T)$ model, while simultaneously describing magnetization rotation and saturation processes that the AS model cannot capture.

IV. CONCLUSIONS

In conclusion, the temperature evolution of uniaxial magnetocrystalline anisotropy has been studied on carefully designed samples that allowed us to directly compare experimental results with thermodynamic descriptions of magnetic anisotropy. Specifically, we observed significant anisotropy to persist close to and above T_C, which is incompatible with the conventional thermodynamic description based on temperature-dependent anisotropy constants $K_n(T)$. High-temperature approximations based on anisotropic susceptibility are also not appropriate in the vicinity of T_C. The VMFA model described here, which stems from a more accurate calculation of the temperature and field-dependent free energy for an appropriate microscopic Hamiltonian, captures all relevant magnetization processes simultaneously, including coherent magnetization rotation and nonvanishing longitudinal susceptibility, and thus fully explains our experimental data. The limiting cases of this VMFA model at low and high T are the $K(T)$ and AS models, respectively. The mathematical expressions for the free energy and magnetization within the VMFA are relatively simple, so that they can be easily and broadly applied in all studies, in which temperatures near T_C can occur, and for which traditional models fail [50]. While having focused here on first-order uniaxial anisotropy effects, the model can easily be extended to account for higher-order anisotropy constants or other symmetries altogether.

ACKNOWLEDGMENTS

We acknowledge support from the Spanish Ministry of Science and Innovation under the Maria de Maeztu Units of Excellence Programme (Grant No. MDM-2016-0618) and Projects No. FIS2015-64519-R (MINECO/FEDER) and No.

RTI2018-094881-B-100 (MCIU/Feder). P. R. acknowledges "la Caixa" Foundation for her Ph.D. fellowship.

APPENDIX: VECTOR MEAN-FIELD APPROXIMATION

1. Derivation of the vector mean-field approximation

Starting with the energy density Hamiltonian in Eq. (4) in Sec. III,

$$\mathcal{H} = -\frac{1}{N}\sum_{i<j}^{N,N} J\boldsymbol{S}_i\cdot\boldsymbol{S}_j + \frac{1}{N}\sum_{i}^{N}\kappa\left[1-\left(S_i^z\right)^2\right] - \frac{\mu_0 M_s^0}{N}\sum_{i}^{N}\boldsymbol{H}\cdot\boldsymbol{S}_i, \tag{A1}$$

we make the substitution

$$\boldsymbol{S}_i = \langle\boldsymbol{S}_i\rangle + \delta\boldsymbol{S}_i, \tag{A2}$$

where $\langle\boldsymbol{S}_i\rangle$ is the thermal expectation value of the spin operator $\boldsymbol{S}_i$ and $\delta\boldsymbol{S}_i$ are fluctuations. The substitution leads to

$$\begin{aligned}\boldsymbol{S}_i\cdot\boldsymbol{S}_j &= (\langle\boldsymbol{S}_i\rangle+\delta\boldsymbol{S}_i)\cdot(\langle\boldsymbol{S}_j\rangle+\delta\boldsymbol{S}_j)\\ &= \langle\boldsymbol{S}_i\rangle\cdot\langle\boldsymbol{S}_j\rangle + \langle\boldsymbol{S}_i\rangle\cdot\delta\boldsymbol{S}_j + \langle\boldsymbol{S}_j\rangle\cdot\delta\boldsymbol{S}_i + \delta\boldsymbol{S}_i\cdot\delta\boldsymbol{S}_j.\end{aligned} \tag{A3}$$

Within the MFA, fluctuations are assumed to be small, so terms that are higher than first order in the fluctuations are neglected, i.e., the term $\delta\boldsymbol{S}_i\delta\boldsymbol{S}_j$ is neglected, leading to

$$\begin{aligned}(\boldsymbol{S}_i\cdot\boldsymbol{S}_j)^{\mathrm{MFA}} &= \langle\boldsymbol{S}_i\rangle\cdot\langle\boldsymbol{S}_j\rangle + \langle\boldsymbol{S}_i\rangle\cdot(\boldsymbol{S}_j-\langle\boldsymbol{S}_j\rangle)\\ &\quad + \langle\boldsymbol{S}_j\rangle\cdot(\boldsymbol{S}_i-\langle\boldsymbol{S}_i\rangle)\\ &= \langle\boldsymbol{S}_i\rangle\cdot\langle\boldsymbol{S}_j\rangle + \langle\boldsymbol{S}_i\rangle\cdot\boldsymbol{S}_j - \langle\boldsymbol{S}_i\rangle\cdot\langle\boldsymbol{S}_j\rangle\\ &\quad + \langle\boldsymbol{S}_j\rangle\cdot\boldsymbol{S}_i - \langle\boldsymbol{S}_i\rangle\cdot\langle\boldsymbol{S}_j\rangle\\ &= -\langle\boldsymbol{S}_i\rangle\cdot\langle\boldsymbol{S}_j\rangle + \langle\boldsymbol{S}_i\rangle\cdot\boldsymbol{S}_j + \langle\boldsymbol{S}_j\rangle\cdot\boldsymbol{S}_i.\end{aligned} \tag{A4}$$

Furthermore,

$$\begin{aligned}\left(S_i^z\right)^2 &= (\hat{\mathrm{z}}\cdot\boldsymbol{S}_i)^2 = (\hat{\mathrm{z}}\cdot(\langle\boldsymbol{S}_i\rangle+\delta\boldsymbol{S}_i))^2\\ &= (\hat{\mathrm{z}}\cdot\langle\boldsymbol{S}_i\rangle + \hat{\mathrm{z}}\cdot\delta\boldsymbol{S}_i)(\hat{\mathrm{z}}\cdot\langle\boldsymbol{S}_i\rangle + \hat{\mathrm{z}}\cdot\delta\boldsymbol{S}_i)\\ &= (\hat{\mathrm{z}}\cdot\langle\boldsymbol{S}_i\rangle)^2 + 2(\hat{\mathrm{z}}\cdot\langle\boldsymbol{S}_i\rangle)(\hat{\mathrm{z}}\cdot\delta\boldsymbol{S}_i) + (\hat{\mathrm{z}}\cdot\delta\boldsymbol{S}_i)^2.\end{aligned} \tag{A5}$$

Again, neglecting terms of second order or higher in $\delta\boldsymbol{S}_i$, i.e., the last term, $(\hat{\mathrm{z}}\cdot\delta\boldsymbol{S}_i)^2$, we derive the MFA equivalent representation

$$\begin{aligned}(S_i^z)^2_{\mathrm{MFA}} &= (\hat{\mathrm{z}}\cdot\langle\boldsymbol{S}_i\rangle)^2 + 2(\hat{\mathrm{z}}\cdot\langle\boldsymbol{S}_i\rangle)(\hat{\mathrm{z}}\cdot(\boldsymbol{S}_i-\langle\boldsymbol{S}_i\rangle))\\ &= (\hat{\mathrm{z}}\cdot\langle\boldsymbol{S}_i\rangle)^2 + 2(\hat{\mathrm{z}}\cdot\langle\boldsymbol{S}_i\rangle)(\hat{\mathrm{z}}\cdot\boldsymbol{S}_i) - 2(\hat{\mathrm{z}}\cdot\langle\boldsymbol{S}_i\rangle)^2\\ &= -(\hat{\mathrm{z}}\cdot\langle\boldsymbol{S}_i\rangle)^2 + 2(\hat{\mathrm{z}}\cdot\langle\boldsymbol{S}_i\rangle)(\hat{\mathrm{z}}\cdot\boldsymbol{S}_i).\end{aligned} \tag{A6}$$

Thus, in the VMFA, which is the vector component-resolved version of the MFA, terms of $\mathcal{O}(\delta\boldsymbol{S}_i\delta\boldsymbol{S}_j)$ and $\mathcal{O}(\delta\boldsymbol{S}_i^2)$ are neglected, so that both, the intersite correlations of fluctuations, $\delta\boldsymbol{S}_i\delta\boldsymbol{S}_j$, and the intrasite ones, $\delta\boldsymbol{S}_i^2$, are assumed to be small. With these approximations, Eq. (A1) can be rewritten as

$$\begin{aligned}\mathcal{H}_{\mathrm{VMFA}} = \frac{1}{2N}\sum_{i,j}^{N,N} J_{ij}\langle\boldsymbol{S}_i\rangle\cdot\langle\boldsymbol{S}_j\rangle - \frac{1}{2N}\sum_{i,j}^{N,N} J_{ij}(\langle\boldsymbol{S}_j\rangle\cdot\boldsymbol{S}_i\\ + \langle\boldsymbol{S}_i\rangle\cdot\boldsymbol{S}_j) + \frac{1}{N}\sum_{i}^{N}\kappa[1+(\hat{\mathrm{z}}\cdot\langle\boldsymbol{S}_i\rangle)^2]\\ - \frac{2}{N}\sum_{i}^{N}\kappa(\hat{\mathrm{z}}\cdot\langle\boldsymbol{S}_i\rangle)(\hat{\mathrm{z}}\cdot\boldsymbol{S}_i) - \frac{\mu_0 M_s^0}{N}\sum_{i}^{N}\boldsymbol{H}\cdot\boldsymbol{S}_i,\end{aligned} \tag{A7}$$

or equivalently

$$\begin{aligned}\mathcal{H}_{\mathrm{VMFA}} = \frac{1}{2N}\sum_{i,j}^{N,N} J_{ij}\langle\boldsymbol{S}_i\rangle\cdot\langle\boldsymbol{S}_j\rangle + \frac{1}{N}\sum_{i}^{N}\kappa(1+(\hat{\mathrm{z}}\cdot\langle\boldsymbol{S}_i\rangle)^2)\\ - \frac{1}{N}\sum_{i}^{N}\boldsymbol{H}_i^{\mathrm{eff}}\cdot\boldsymbol{S}_i\end{aligned} \tag{A8}$$

$$\text{with}\quad \boldsymbol{H}_i^{\mathrm{eff}} = \sum_{j}^{N} J_{ij}\,\langle\boldsymbol{S}_j\rangle + 2\kappa(\hat{\mathrm{z}}\cdot\langle\boldsymbol{S}_i\rangle)\hat{\mathrm{z}} + \mu_0 M_s^0\boldsymbol{H}. \tag{A9}$$

Utilizing translational invariance and considering only nearest-neighbor interactions, we find

$$\mathcal{H}_{\mathrm{VMFA}} = \tfrac{1}{2}\,q\,J\langle\boldsymbol{S}\rangle^2 + \kappa(1+(\hat{\mathrm{z}}\cdot\langle\boldsymbol{S}\rangle)^2) - \boldsymbol{H}^{\mathrm{eff}}\cdot\boldsymbol{S}, \tag{A10}$$

$$\text{with}\quad \boldsymbol{H}^{\mathrm{eff}} = q\,J\langle\boldsymbol{S}\rangle + 2\kappa(\hat{\mathrm{z}}\cdot\langle\boldsymbol{S}\rangle)\hat{\mathrm{z}} + \mu_0 M_s^0\boldsymbol{H}, \tag{A11}$$

where q is the number of nearest neighbors. In a quantum-mechanical picture, $\boldsymbol{S}$ is the spin operator. In the classical approach that will be utilized in the following, it is a spin vector with fixed modulus and components S_x, S_y, and S_z. Given that uniaxial anisotropy is considered, one can restrict the analysis of the averages to the plane that contains the field vector and the EA, which we define as the xz plane. The EA is along the z axis, so S_z will be represented as $S_\parallel$, and S_x as $S_\perp$. Thus, the components of $\boldsymbol{H}^{\mathrm{eff}}$ are

$$H_\perp^{\mathrm{eff}} = qJ\langle S_\perp\rangle + \mu_0 M_s^0 H\sin\alpha, \tag{A12}$$

$$H_\parallel^{\mathrm{eff}} = q\,J\langle S_\parallel\rangle + \mu_0 M_s^0 H\cos\alpha + 2\kappa\langle S_\parallel\rangle, \tag{A13}$$

where α is the angle between the applied field axis and the easy axis, and H is the amplitude of the applied field. The partition function of the system is

$$\mathcal{Z} = \sum_{\{\boldsymbol{S}\}}\exp\left(-\beta\mathcal{H}_{\mathrm{VMFA}}\right), \tag{A14}$$

and the free energy

$$\begin{aligned}\mathcal{F}_{\mathrm{VMFA}} &= -\frac{1}{\beta}\ln\mathcal{Z}\\ &= \frac{1}{2}\,q\,J\langle\boldsymbol{S}\rangle^2 + \kappa\,(1+(\hat{\mathrm{z}}\cdot\langle\boldsymbol{S}\rangle)^2)\\ &\quad - \frac{1}{\beta}\ln\sum_{\{\boldsymbol{S}\}}\exp(\beta\,\boldsymbol{H}^{\mathrm{eff}}\cdot\boldsymbol{S})\end{aligned} \tag{A15}$$

with $\beta = \frac{1}{k_B T}$. In spherical coordinates, one can write

$$\boldsymbol{H}^{\text{eff}} \cdot \boldsymbol{S} = |\boldsymbol{H}^{\text{eff}}||\boldsymbol{S}| \cos\theta = H^{\text{eff}} \cos\theta, \tag{A16}$$

where θ is the angle between the spins and the effective field. The sum in the last term can be written as an integral over all orientations that yields

$$\begin{aligned}\sum_{\{\boldsymbol{S}\}} &\exp(\beta\, \boldsymbol{H}^{\text{eff}} \cdot \boldsymbol{S}) \\ &= \frac{1}{4\pi} \int_0^{2\pi} d\varphi \int_0^{\pi} \exp\left(\beta H^{\text{eff}} \cos\theta\right) \sin\theta\, d\theta \\ &= \frac{\sinh\left(\beta H^{\text{eff}}\right)}{\beta H^{\text{eff}}} \equiv \mathcal{Z}_0 \end{aligned} \tag{A17}$$

with

$$H^{\text{eff}} = \sqrt{(H_\perp^{\text{eff}})^2 + (H_\parallel^{\text{eff}})^2}. \tag{A18}$$

So, $\mathcal{F}_{\text{VMFA}}$ is given by

$$\begin{aligned}\mathcal{F}_{\text{VMFA}} = &\frac{1}{2}\, qJ\langle \boldsymbol{S}\rangle^2 + \kappa\, (1 + (\hat{\mathrm{z}} \cdot \langle \boldsymbol{S}\rangle)^2) \\ &- \frac{1}{\beta} \ln\left(\frac{\sinh\left(\beta H^{\text{eff}}\right)}{\beta H^{\text{eff}}}\right). \end{aligned} \tag{A19}$$

The components of the magnetization are obtained by means of $M_\nu = -\frac{\partial \mathcal{F}}{\partial(\mu_0 H_\nu)}$, where $\nu = \perp, \parallel$. Useful relations for the calculation of M_ν are

$$\frac{\partial H^{\text{eff}}}{\partial(\mu_0 H_\perp)} = M_s^0 \frac{H_\perp^{\text{eff}}}{H^{\text{eff}}}; \quad \frac{dH^{\text{eff}}}{d(\mu_0 H_\parallel)} = M_s^0 \frac{H_\parallel^{\text{eff}}}{H^{\text{eff}}}, \tag{A20}$$

which lead to

$$\begin{aligned}\frac{M_\perp}{M_s^0} = \langle S_\perp\rangle &= -\frac{1}{M_s^0} \frac{\partial \mathcal{F}}{\partial(\mu_0 H_\perp)} = -\frac{1}{M_s^0} \frac{\partial \mathcal{F}}{\partial H^{\text{eff}}} \frac{\partial H^{\text{eff}}}{\partial(\mu_0 H_\perp)} \\ &= \frac{1}{\beta} \frac{1}{\mathcal{Z}_0} \left[\frac{\beta^2 H^{\text{eff}} \cosh\left(\beta H^{\text{eff}}\right) - \beta \sinh\left(\beta H^{\text{eff}}\right)}{\left(\beta H^{\text{eff}}\right)^2}\right] \frac{H_\perp^{\text{eff}}}{H^{\text{eff}}} \\ &= \left(\coth(\beta H^{\text{eff}}) - \frac{1}{\beta H^{\text{eff}}}\right) \frac{H_\perp^{\text{eff}}}{H^{\text{eff}}}. \end{aligned} \tag{A21}$$

In the same way, we find

$$\frac{M_\parallel}{M_s^0} = \langle S_\parallel\rangle = \left(\coth(\beta H^{\text{eff}}) - \frac{1}{\beta H^{\text{eff}}}\right) \frac{H_\parallel^{\text{eff}}}{H^{\text{eff}}}, \tag{A22}$$

which completes the derivation of Eq. (8) in Sec. III. Since H^{eff} depends on $\langle S_\perp\rangle$ and $\langle S_\parallel\rangle$, Eqs. (A21) and (A22) are coupled and need to be solved self-consistently. By doing so as a function of H and α for different temperatures T one can compute the type of magnetization maps that are shown in Figs. 3(a)–3(c), where the magnitude displayed in color code is the field-projected magnetization $\langle S_\parallel\rangle \cos\alpha + \langle S_\perp\rangle \sin\alpha$.

2. Determination of T_c and high-temperature limit

In the vicinity of T_c and in the absence of a magnetic field, the magnetization is small, so that $\beta H^{\text{eff}} \ll 1$ is fulfilled. Making use of the Taylor expansion of $\sinh(x)$ and of $\ln(1+x)$, the H^{eff}-dependent part of $\mathcal{F}_{\text{VMFA}}$ reduces to

$$\begin{aligned}\mathcal{F} &= -\frac{1}{\beta} \text{Ln}\left(\frac{\sinh\left(\beta H^{\text{eff}}\right)}{\beta H^{\text{eff}}}\right) \\ &\approx -\frac{1}{\beta} \text{Ln}\left(1 + \frac{1}{6}(\beta H^{\text{eff}})^2\right) \approx -\frac{1}{6} \beta H^{\text{eff}^2}, \end{aligned} \tag{A23}$$

from which follows

$$\frac{M_\parallel}{M_s^0} = \langle S_\parallel\rangle = \frac{1}{3} \beta H_\parallel^{\text{eff}}, \tag{A24}$$

$$\frac{M_\perp}{M_s^0} = \langle S_\perp\rangle = \frac{1}{3} \beta H_\perp^{\text{eff}}. \tag{A25}$$

Near T_c, the magnetization will be aligned near the z axis for small H, and in the $H \to 0$ limit it will be parallel to z. From Eq. (A24) we derive for the limit $H \to 0$ that

$$\langle S_\parallel\rangle = \frac{\beta \langle S_\parallel\rangle}{3} (qJ\ + 2\kappa\ ) \to \langle S_\parallel\rangle \left(1 - \frac{\beta}{3}(qJ + 2\kappa)\right) = 0. \tag{A26}$$

At T_c the term in the parentheses vanishes, from which we obtain

$$T_c = \frac{1}{3k_B}(qJ + 2\kappa). \tag{A27}$$

The $\beta H^{\text{eff}} \ll 1$ approximation is valid for low magnetization values. This is the case near T_c for very small H values only, but for higher temperatures the H range increases, for which the approximation is valid, because a small H is not sufficient to induce relevant magnetization levels. Thus, one can use Eqs. (A24) and (A25) to determine the field dependence of the magnetization at high T. By solving for $\langle S_\perp\rangle$ and $\langle S_\parallel\rangle$, we find

$$\frac{M_\perp}{M_s^0} = \langle S_\perp\rangle = \frac{1}{(3k_B T - q\, J)} H_\perp \equiv \chi_\perp H_\perp, \tag{A28}$$

$$\frac{M_\parallel}{M_s^0} = \langle S_\parallel\rangle = \frac{1}{(3k_B T - q\, J - 2\kappa)} H_\parallel \equiv \chi_\parallel H_\parallel. \tag{A29}$$

Equations (A28) and (A29) show that the magnetization components are proportional to the field components with different temperature-dependent proportionality factors, i.e., susceptibilities, along the easy and hard axes, meaning that the anisotropic susceptibility model is obtained in the $\beta H^{\text{eff}} \ll 1$ limit. Using Eq. (A27) one can see that the longitudinal susceptibility $\chi_\parallel$ diverges at T_c while $\chi_\perp$ remains finite. Finally, Eqs. (A28) and (A29) enable us to write the free energy in the high-temperature limit as

$$\mathcal{F}_{\text{AS}} = -\frac{\mu_0 M_s^0}{2} \chi_\parallel(T) H_\parallel^2 - \frac{\mu_0 M_s^0}{2} \chi_\perp(T) H_\perp^2, \tag{A30}$$

and thus enable us to reproduce Eq. (3) of the main text.

3. Low-temperature behavior and proper refinement

In order to determine the M dependence of the phenomenological $K(T)$ resulting from the VMFA model and verify whether it satisfies the Callen-Callen law, which predicts $K(T) \sim M^3$ at low temperatures for uniaxial anisotropy, the VMFA model is compared to the macrospin $K(T)$ model. The phenomenological expression for the macrospin free energy is considered

$$\mathcal{F}_{K(T)} = -\mu_0 M_s(T)\hat{\boldsymbol{m}} \cdot \boldsymbol{H} - K(T)(\hat{\boldsymbol{m}} \cdot \hat{\boldsymbol{z}})^2. \tag{A31}$$

Taking $\boldsymbol{H}$ to lie perpendicular to the EA, we have

$$\mathcal{F}_{K(T)} = -\mu_0 M_s(T) H \sin\theta_z - K(T)\cos^2\theta_z, \tag{A32}$$

where θ_z is the angle between the EA (z) and the magnetization. To obtain the equilibrium condition, $\mathcal{F}_{K(T)}$ is differentiated with respect to θ_z and is set to zero:

$$\frac{\partial \mathcal{F}_{K(T)}}{\partial \theta_z} = 2K\cos\theta_z \sin\theta_z - \mu_0 M_s H \cos\theta_z = 0. \tag{A33}$$

The equilibrium magnetization orientation is thus given by

$$\sin\theta_z = \frac{\mu_0 M_s H}{2K} = \frac{\mu_0 H M_s^0 \langle S\rangle}{2K}. \tag{A34}$$

Let us compare Eq. (A34) with the equilibrium magnetization angle obtained from Eq. (A19), representing the VMFA, again assuming that $\boldsymbol{H}$ is perpendicular to the EA:

$$\frac{\partial \mathcal{F}_{\mathrm{VMFA}}}{\partial \theta_z} = qJ\langle S\rangle \frac{\partial \langle S\rangle}{\partial \theta_z} + 2\kappa\cos^2\theta_z \langle S\rangle \frac{\partial \langle S\rangle}{\partial \theta_z} - 2\kappa\cos\theta_z \sin\theta_z \langle S\rangle^2 - \langle S\rangle \frac{\partial H^{\mathrm{eff}}}{\partial \theta_z}. \tag{A35}$$

From Eqs. (A12) and (A13), and assuming that $\mu_0 M_s^0 H \ll qJ$ and $\kappa \ll qJ$, we find

$$\begin{aligned} H^{\mathrm{eff}} &\approx \sqrt{(qJ)^2\langle S\rangle^2 + 4qJ\kappa\langle S\rangle^2\cos^2\theta_z + 2qJ\mu_0 M_s^0 H\langle S\rangle\sin\theta_z} \\ &= qJ\langle S\rangle\sqrt{1 + \left(\frac{4\kappa}{qJ}\cos^2\theta_z + \frac{2\mu_0 M_s^0 H}{qJ\langle S\rangle}\sin\theta_z\right)} \\ &\approx (qJ + 2\kappa\cos^2\theta_z)\langle S\rangle + \mu_0 M_s^0 H\sin\theta_z, \end{aligned} \tag{A36}$$

so that

$$\frac{\partial H^{\mathrm{eff}}}{\partial \theta_z} = qJ\frac{\partial \langle S\rangle}{\partial \theta_z} - 4\kappa\langle S\rangle\cos\theta_z\sin\theta_z + 2\kappa\cos^2\theta_z\frac{\partial\langle S\rangle}{\partial\theta_z} + \mu_0 M_s^0 H\cos\theta_z. \tag{A37}$$

Thus, the equilibrium condition is

$$\frac{\partial \mathcal{F}_{\mathrm{VMFA}}}{\partial \theta_z} = 2\kappa\langle S\rangle^2\cos\theta_z\sin\theta_z - \mu_0 M_s^0 H\langle S\rangle\cos\theta_z = 0, \tag{A38}$$

from which

$$\sin\theta_z = \frac{\mu_0 M_s^0 H}{2\kappa\langle S\rangle} \tag{A39}$$

follows. If we compare Eq. (A39) to Eq. (A34), we see that

$$K(T) = \kappa\langle S\rangle^2 \sim M^2, \tag{A40}$$

and therefore, the Callen-Callen law is not satisfied in the VMFA approximation. However, this very low-temperature effect can be overcome if intersite fluctuation correlation effects $\mathcal{O}(\delta \boldsymbol{S}_i \delta \boldsymbol{S}_j)$ are neglected, but intrasite ones, $\mathcal{O}(\delta \boldsymbol{S}_i^2)$, are taken into consideration, i.e., if the MFA is applied to the exchange energy term, but not to the anisotropy energy term. In this case, the MFA Hamiltonian can be expressed as follows, after considering nearest-neighbor interactions and translational invariance:

$$\tilde{\mathcal{H}}_{\mathrm{MFA}} = \tfrac{1}{2}qJ\langle \boldsymbol{S}\rangle^2 + \kappa - \kappa(S_z)^2 - \tilde{\boldsymbol{H}}^{\mathrm{eff}} \cdot \boldsymbol{S}, \tag{A41}$$

with

$$\tilde{\boldsymbol{H}}^{\mathrm{eff}} = qJ\langle \boldsymbol{S}\rangle + \mu_0 M_s^0 \boldsymbol{H}. \tag{A42}$$

Thus, the free energy has the form

$$\begin{aligned} \tilde{\mathcal{F}}_{\mathrm{MFA}} &= -\frac{1}{\beta}\ln\mathcal{Z} \\ &= \frac{1}{2}qJ\langle \boldsymbol{S}\rangle^2 + \kappa \\ &\quad - \frac{1}{\beta}\ln\left(\sum_{\{S\}}\exp\left(\beta\left(\tilde{\boldsymbol{H}}^{\mathrm{eff}} \cdot \boldsymbol{S} + \kappa S_z^2\right)\right)\right). \end{aligned} \tag{A43}$$

In order to carry out the spin-state integration explicitly, an approximation of small anisotropy $\beta\kappa \ll 1$ is applied, namely

$$\exp\left(\beta\left(\tilde{\boldsymbol{H}}^{\mathrm{eff}} \cdot \boldsymbol{S} + \kappa S_z^2\right)\right) \approx \exp(\beta\tilde{\boldsymbol{H}}^{\mathrm{eff}} \cdot \boldsymbol{S})\left(1 + \beta\kappa S_z^2\right). \tag{A44}$$

The logarithm term in Eq. (A43) can be thus be rewritten and separated, so that

$$\begin{aligned} &\ln\left(\sum_{\{S\}}\left(1 + \beta\kappa S_z^2\right)\exp(\beta\tilde{\boldsymbol{H}}^{\mathrm{eff}} \cdot \boldsymbol{S})\right) \\ &\quad = \ln\left(\sum_{\{S\}}\exp(\beta\tilde{\boldsymbol{H}}^{\mathrm{eff}} \cdot \boldsymbol{S}) + \sum_{\{S\}}\beta\kappa S_z^2\exp(\beta\tilde{\boldsymbol{H}}^{\mathrm{eff}} \cdot \boldsymbol{S})\right). \end{aligned} \tag{A45}$$

We already demonstrated that

$$\sum_{\{S\}}\exp(\beta \boldsymbol{S}\tilde{\boldsymbol{H}}^{\mathrm{eff}}) = \frac{\sinh(\beta\tilde{H}^{\mathrm{eff}})}{\beta\tilde{H}^{\mathrm{eff}}} \equiv \tilde{\mathcal{Z}}_0, \tag{A46}$$

where $\tilde{H}^{\text{eff}}$ is the magnitude of $\tilde{\boldsymbol{H}}^{\text{eff}}$. Thus, we only need to compute

$$\sum_{\{S\}} \beta\kappa S_z^2 \exp(\beta\tilde{\boldsymbol{H}}^{\text{eff}} \cdot \boldsymbol{S}) = \frac{1}{4\pi}\int_0^{2\pi} d\varphi \int_0^{\pi} \beta\kappa \cos^2\theta_z \exp(\beta\tilde{H}^{\text{eff}} \cos\theta) \sin\theta \, d\theta \tag{A47}$$

to determine the free energy according to Eq. (A43). Taking into account that $S_z^2 = \cos^2\theta_z$, where θ_z is the angle between the spin and the anisotropy axis, and θ is the angle between $\boldsymbol{S}$ and $\tilde{\boldsymbol{H}}^{\text{eff}}$, one can rewrite the integral by using the auxiliary angle $\tilde{\theta}$, which is the angle between $\tilde{\boldsymbol{H}}^{\text{eff}}$ and the anisotropy axis z.

The result yields

$$\sum_{\{S\}} \beta\kappa S_z^2 \exp(\beta\tilde{\boldsymbol{H}}^{\text{eff}} \cdot \boldsymbol{S}) = \beta\kappa \tilde{\mathcal{Z}}_0 f, \tag{A48}$$

with

$$f = \cos^2\tilde{\theta} + (1 - 3\cos^2\tilde{\theta}) \frac{1}{\beta\tilde{H}^{\text{eff}}} \left(\coth(\beta\tilde{H}^{\text{eff}}) - \frac{1}{\beta\tilde{H}^{\text{eff}}} \right). \tag{A49}$$

The free energy can be written as

$$\tilde{\mathcal{F}}_{\text{MFA}} = \frac{1}{2} qJ\langle \boldsymbol{S} \rangle^2 + \kappa - \frac{1}{\beta} \ln(\tilde{\mathcal{Z}}_0(1 + \beta\kappa f)), \tag{A50}$$

which can be further simplified to

$$\tilde{\mathcal{F}}_{\text{MFA}} = \frac{1}{2} qJ\langle \boldsymbol{S} \rangle^2 - \frac{1}{\beta} \ln(\tilde{\mathcal{Z}}_0) + \kappa(1 - f), \tag{A51}$$

taking again advantage of the assumption $\beta\kappa \ll 1$. Following the procedure in part 1 of the Appendix, the expressions for the spin components are

$$\langle S_\perp \rangle = \frac{\tilde{H}_\perp^{\text{eff}}}{\tilde{H}^{\text{eff}}} A + f_\perp B, \tag{A52}$$

$$\langle S_\parallel \rangle = \frac{\tilde{H}_\parallel^{\text{eff}}}{\tilde{H}^{\text{eff}}} A + f_\parallel B, \tag{A53}$$

with

$$A = d_{\text{eff}} \left(1 + 3\frac{f_0\tilde{\kappa}}{h_{\text{eff}}} \right) - 3f_0\tilde{\kappa} \left(1 - (c_{\text{eff}})^2 + \frac{1}{(h_{\text{eff}})^2} \right), \tag{A54}$$

$$B = \left(1 - 3\frac{d_{\text{eff}}}{h_{\text{eff}}} \right) \bar{\tilde{\kappa}}, \tag{A55}$$

$$d_{\text{eff}} = c_{\text{eff}} - \frac{1}{h_{\text{eff}}}, \tag{A56}$$

$$c_{\text{eff}} = \coth(h_{\text{eff}}), \tag{A57}$$

$$\tilde{\kappa} = \frac{\kappa}{\tilde{H}^{\text{eff}}}, \tag{A58}$$

$$\bar{\tilde{\kappa}} = \frac{\kappa}{qJ}, \tag{A59}$$

$$h_{\text{eff}} = \beta\tilde{H}^{\text{eff}}, \tag{A60}$$

$$f_\perp = -2\frac{\langle S_\parallel \rangle^2 \langle S_\perp \rangle}{(\langle S_\perp \rangle^2 + \langle S_\parallel \rangle^2)^2}, \tag{A61}$$

$$f_\parallel = 2\frac{\langle S_\perp \rangle^2 \langle S_\parallel \rangle}{(\langle S_\perp \rangle^2 + \langle S_\parallel \rangle^2)^2}, \tag{A62}$$

$$f_0 = \frac{\langle S_\parallel \rangle^2}{\langle S_\perp \rangle^2 + \langle S_\parallel \rangle^2}. \tag{A63}$$

This is a refined version of the VMFA model and at the temperatures of interest in the experiments, which are close to T_c, it is basically equivalent to the VMFA model presented earlier. Utilizing this refined model, we derive from Eq. (A51) that

$$\begin{aligned} \frac{\partial\tilde{\mathcal{F}}_{\text{MFA}}}{\partial\theta_z} &= qJ\langle S \rangle \frac{\partial\langle S \rangle}{\partial\theta_z} - \left(\coth(\beta\tilde{H}^{\text{eff}}) - \frac{1}{\beta\tilde{H}^{\text{eff}}} \right) \frac{\partial\tilde{H}^{\text{eff}}}{\partial\theta_z} \\ &\quad - \kappa\frac{\partial f}{\partial\theta_z} \\ &= qJ\langle S \rangle \frac{\partial\langle S \rangle}{\partial\theta_z} - \left(\langle S \rangle - \kappa\frac{\partial f}{\partial\tilde{H}^{\text{eff}}} \right) \frac{\partial\tilde{H}^{\text{eff}}}{\partial\theta_z} - \kappa\frac{\partial f}{\partial\theta_z}. \end{aligned} \tag{A64}$$

Using the same approximations as for Eq. (A36) we obtain

$$\frac{\partial\tilde{H}^{\text{eff}}}{\partial\theta_z} = qJ\frac{\partial\langle S \rangle}{\partial\theta_z} + \mu_0 M_s^0 H \cos\theta_z. \tag{A65}$$

On the other hand

$$\begin{aligned} \frac{\partial f}{\partial\theta_z} &= -2\cos\theta_z \sin\theta_z + 6\cos\theta_z \sin\theta_z \left(\langle S \rangle - \kappa\frac{\partial f}{\partial\tilde{H}^{\text{eff}}} \right) \\ &\quad \times \frac{1}{\beta\tilde{H}^{\text{eff}}} + \frac{\partial f}{\partial\tilde{H}^{\text{eff}}} \frac{\partial\tilde{H}^{\text{eff}}}{\partial\theta_z}, \end{aligned} \tag{A66}$$

from which follows that

$$\begin{aligned} \frac{\partial\tilde{\mathcal{F}}_{\text{MFA}}}{\partial\theta_z} &= -\mu_0 M_s^0 H\langle S \rangle \cos\theta_z + 2\kappa \cos\theta_z \sin\theta_z \\ &\quad \times \left(1 - \frac{3\langle S \rangle}{\beta\tilde{H}^{\text{eff}}} (1 - \gamma) \right), \end{aligned} \tag{A67}$$

with $\gamma = \frac{\kappa}{\langle S \rangle} \frac{\partial f}{\partial\tilde{H}^{\text{eff}}} \ll 1$. In equilibrium, Eq. (A67) needs to be equal to zero, so that

$$\sin\theta_z = \frac{\mu_0 M_s^0 H\langle S \rangle}{2\kappa\left(1 - \frac{3\langle S \rangle}{\beta\tilde{H}^{\text{eff}}}(1 - \gamma)\right)} \approx \frac{\mu_0 M_s^0 H\langle S \rangle}{2\kappa\left(1 - \frac{3\langle S \rangle}{\beta\tilde{H}^{\text{eff}}}\right)}. \tag{A68}$$

When compared to Eq. (A34), one can identify

$$K(T) = \kappa\left(1 - \frac{3\langle S \rangle}{\beta\tilde{H}^{\text{eff}}} \right), \tag{A69}$$

which for low temperatures can be written as $K(T) \sim \langle S \rangle^3$, thus recovering the Callen-Callen law.

[1] J. H. van Vleck, Phys. Rev. **52**, 1178 (1937).
[2] H. Brooks, Phys. Rev. **58**, 909 (1940).
[3] J. M. D. Coey, *Magnetism and Magnetic Materials* (Cambridge University Press, Cambridge, UK, 2010).
[4] M. E. Fisher, Rev. Mod. Phys. **46**, 597 (1974).
[5] N. Akulov, Z. Phys. **100**, 197 (1936).
[6] C. Zener, Phys. Rev. **96**, 1335 (1954).
[7] H. B. Callen and E. Callen, J. Phys. Chem. Solids **27**, 1271 (1966).
[8] Y. Millev and M Fähnle, Phys. Rev. B **52**, 4336 (1995).
[9] J. B. Staunton, S. Ostanin, S. S. A. Razee, B. L. Gyorffy, L. Szunyogh, B. Ginatempo, and E. Bruno, Phys. Rev. Lett. **93**, 257204 (2004).
[10] R. Skomski, O. N. Mryasov, J. Zhou, and D. J. Sellmyer, J. Appl. Phys. **99**, 08E916 (2006).
[11] I. A. Zhuravlev, V. P. Antropov, and K. D. Belashchenko, Phys. Rev. Lett. **115**, 217201 (2015).
[12] M. Stier, A. Neumann, A. Kobs, H. P. Oepen, and M. Thorwart, J. Magn. Magn. Mater. **447**, 96 (2018).
[13] J. J. M. Franse and G. De Vries, Physica **39**, 477 (1968).
[14] D. M. Paige, B. Szpunar, and B. K. Tanner, J. Magn. Magn. Mater. **44**, 239 (1984).
[15] J.-U. Thiele, K. R. Coffey, M. F. Toney, J. A. Hedstrom, and A. J. Kellock, J. Appl. Phys. **91**, 6595 (2002).
[16] N. D. Mermin and H. Wagner, Phys. Rev. Lett. **17**, 1133 (1966).
[17] M. Bander and D. L. Mills, Phys. Rev. B **38**, 12015(R) (1988).
[18] C. Gong, L. Li, Z. Li, H. Ji, A. Stern, Y. Xia, T. Cao, W. Bao, C. Wang, Y. Wang, Z. Q. Qiu, R. J. Cava, S. G. Louie, J. Xia, and X. Zhang, Nature (London) **546**, 265 (2017).
[19] B. Huang, G. Clark, E. Navarro-Moratalla, D. R. Klein, R. Cheng, K. L. Seyler, D. Zhong, E. Schmidgall, M. A. McGuire, D. H. Cobden, W. Yao, D. Xiao, P. Jarillo-Herrero, and X. Xu, Nature (London) **546**, 270 (2017).
[20] J. M. D. Coey, IEEE Trans. Magn. **47**, 4671 (2011).
[21] D. Weller *et al.*, IEEE Trans. Magn. **36**, 10 (2000).
[22] R. Wood, IEEE Trans. Magn. **36**, 36 (2000).
[23] D. Sander, S. O. Valenzuela, D. Makarov, C. H. Marrows, E. E. Fullerton, P. Fischer, J. McCord, P. Vavassori, S. Mangin, P. Pirro, B. Hillebrands, A. D. Kent, T. Jungwirth, O. Gutfleisch, C.-G. Kim, and A. Berger, J. Phys. D: Appl. Phys. **50**, 363001 (2017).
[24] E. Y. Vedmedenko, R. K. Kawakami, D. D. Sheka, P. Gambardella, A. Kirilyuk, A. Hirohata, C. Binek, O. Chubykalo-Fesenko, S. Sanvito, B. J. Kirby, J. Grollier, K. Everschor-Sitte, T. Kampfrath, C-Y. You, and A. Berger, J. Phys. D **53**, 453001 (2020).
[25] Y. Yoshizawa, S. Oguma, and K. Yamauchi, J. Appl. Phys. **64**, 6044 (1988).
[26] M. Hervé, B. Dupé, R. Lopes, M. Böttcher, M. D. Martins, T. Balashov, L. Gerhard, J. Sinova, and W. Wulfhekel, Nat. Commun. **9**, 1015 (2018).
[27] M. N. Wilson, A. B. Butenko, A. N. Bogdanov, and T. L. Monchesky, Phys. Rev. B **89**, 094411 (2014).
[28] U. Bauer, L. Yao, A. J. Tan, P. Agrawal, S. Emori, H. L. Tuller, S. van Dijken, and G S. D. Beach, Nat. Mater. **14**, 174 (2015).
[29] J. B. Staunton, L. Szunyogh, A. Buruzs, B. L. Gyorffy, S. Ostanin, and L. Udvardi, Phys. Rev. B **74**, 144411 (2006).
[30] C. E. Patrick and J. B. Staunton, Phys. Rev. Mater. **3**, 101401(R) (2019).
[31] By including the last term in Eq. (2) we are formally making a transformation from the Helmholtz free energy to the Gibbs free energy.
[32] A. Hubert and R. Schäfer, *Magnetic Domains: the Analysis of Magnetic Microstructures* (Springer, Berlin, 1998).
[33] H. Suzuki and T. Watanabe, J. Phys. Soc. Jpn. **30**, 367 (1971).
[34] P. J. Jensen, S. Knappmann, W. Wulfhekel, and H. P. Oepen, Phys. Rev. B **67**, 184417 (2003).
[35] M. G. Pini, P. Politi, and R. L. Stamps, Phys. Rev. B **72**, 014454 (2005).
[36] S. Tacchi, A. Stollo, M. Madami, G. Gubbiotti, G. Carlotti, M. G. Pini, P. Politi, and R. L. Stamps, Surf. Sci. **600**, 4147 (2006).
[37] *Magnetism*, edited by G. T. Rado and H. Suhl (Academic Press, New York, 1963), Vol. 1.
[38] L. Fallarino, A. Oelschlägel, J. A. Arregi, A. Bashkatov, F. Samad, B. Böhm, K. Chesnel, and O. Hellwig, Phys. Rev. B **99**, 024431 (2019).
[39] L. Fallarino, S. Stienen, R. A. Gallardo, J. A. Arregi, V. Uhlir, K. Lenz, R. Hübner, A. Oelschlägel, O. Hellwig, and J. Lindner, Phys. Rev. B **102**, 094434 (2020).
[40] O. Idigoras, U. Palomares, A. K. Suszka, L. Fallarino, and A. Berger, Appl. Phys. Lett. **103**, 102410 (2013).
[41] L. Fallarino, P. Riego, B. J. Kirby, C. W. Miller, and A. Berger, Materials **11**, 251 (2018).
[42] J. M. Marín Ramírez, E. Oblak, P. Riego, G. Campillo, J. Osorio, O. Arnache, and A. Berger, Phys. Rev. E **102**, 022804 (2020).
[43] M. Quintana, E. Oblak, J. M. Marín Ramírez, and A. Berger, Phys. Rev. B **102**, 094436 (2020).
[44] W. Yang and D. N. Lambeth, J. Appl. Phys. **85**, 4723 (1999).
[45] O. Idigoras, A. K. Suszka, P. Vavassori, B. Obry, B. Hillebrands, P. Landeros, and A. Berger, J. Appl. Phys. **115**, 083912 (2014).
[46] A. Arrott and J. E. Noakes, Phys. Rev. Lett. **19**, 786 (1967).
[47] The numerical $M(T,H)$ results have been determined using the series expansion of the Ising model described by C. Domb, in *Phase Transitions and Critical Phenomena*, edited by C. Domb and M. S. Green (Academic Press, London, 1974), Vol. 3, Chap. 6, pp. 446–449. Without loss of general comparability, the series for $S = 1/2$ was chosen here to compute the inset of Fig. 1(b).
[48] L. Fallarino, B. J. Kirby, M. Pancaldi, P. Riego, A. L. Balk, C. W. Miller, P. Vavassori, and A. Berger, Phys. Rev. B **95**, 134445 (2017).
[49] P. Bruno, Phys. Rev. B **39**, 865(R) (1989).
[50] Only at very low temperatures does the VMFA fail to reproduce the Callen-Callen power law [7]. Refined calculations in the Appendix overcome this limitation.